



HAL
open science

Catalytic Tubular Microjet Navigating in Confined Microfluidic Channels: Modeling and Optimization

Bruno Sarkis, David Folio, Antoine Ferreira

► **To cite this version:**

Bruno Sarkis, David Folio, Antoine Ferreira. Catalytic Tubular Microjet Navigating in Confined Microfluidic Channels: Modeling and Optimization. *Journal of Microelectromechanical Systems*, 2018, 27 (2), pp.333-343. 10.1109/JMEMS.2018.2803803 . hal-03528605

HAL Id: hal-03528605

<https://hal.science/hal-03528605>

Submitted on 14 Oct 2022

HAL is a multi-disciplinary open access archive for the deposit and dissemination of scientific research documents, whether they are published or not. The documents may come from teaching and research institutions in France or abroad, or from public or private research centers.

L'archive ouverte pluridisciplinaire **HAL**, est destinée au dépôt et à la diffusion de documents scientifiques de niveau recherche, publiés ou non, émanant des établissements d'enseignement et de recherche français ou étrangers, des laboratoires publics ou privés.

Catalytic Tubular Microjet Navigating in Confined Microfluidic Channels: Modeling and Optimization

Bruno Sarkis, David Folio and Antoine Ferreira

Abstract—This paper describes the propulsion of the catalytic tubular microjet in confined environments as microchannels and capillaries using the Stokes equations. Especially, the thrust capability of the microjet is outstanding compared with the other microsystems, but remains only partially understood. Studies have identified the internal precursory mechanisms of the propulsion of the microjet: its inner wall catalyzes the dismutation of the fuel, and bubbles are then formed. Since the jet is conical, the bubble migrates towards its widest opening. This impules the propulsion of the microjet towards the opposite direction. However, the precise propellant role of the liquid surrounding the jet remains misunderstood. The same goes for the inner wall of the vessel in which the jet navigates, especially in narrowed environment. This article discusses these aspects in a simplified theoretical framework. Calculations are performed by explicit computation of the Stokes equations. The obtained theoretical results are in good agreement with experimental results reported in the literature.

Index Terms—Catalytic microjet, design, modeling, propulsion, microrobotics.

I. INTRODUCTION

THANKS to their powerful propulsion and as they do not require any external supply of energy (except for their guidance), self-propelled microrobots are a promising nanotechnology for micromanipulation or biomedical applications [1], [2]. Self-propelled microrobots are part of the family of microswimmers, in which several artificial forms of propulsion have been designed such as propulsion by bubbles, electrophoretic, electric, magnetic, acoustic [1], [2]. Among these, the catalytic tubular microjets are particularly attractive due to their forceful propulsion mechanism [3], [4]. They draw their fuel, including water, hydrogen peroxide (H_2O_2), strong acids, hydrazine or glucose, from the surrounding liquid (water or blood medium) and convert it into bubbles of gas (e.g. O_2 or H_2) by catalysis [4]–[10]. Their propulsion is ensured with no external energy supply, which is not the case for other modes of propulsion, as magnetic or acoustic modes [11]. In particular, in [6] the authors have studied the contact with living tissues, and in [12] their control in microfluidic environment with time-varying flow is addressed. Some attempts using stomatocytes previously loaded with platinum nanoparticles and doxorubicin in presence of H_2O_2 secreting neutrophil cells have been carried out successfully in 3D microfluidic channels [6]. For these reasons, catalytic tubular microjets are the most promising ways to propel more massive microsystem for future medical microrobots, delivery

of cargo and many other applications [2], [8]. However, one of the remaining questions is to demonstrate biocompatibility of the fuel and the viability of the bioorganisms at those conditions where catalytic microjets navigate. The utilization of non-toxic fuels by the integration of enzymes as active catalyst (catalase, urease and glucose oxidase) in microjets is actually investigated [10], [13].

To achieve these goals, it is important to understand the propulsion mechanism of the catalytic microjet. Previous studies [2], [5], [7]–[9] have initiated the description of the behavior of the microjet. In particular, its driving motion is different to similar systems such as nanorods. Whereas for nanorods the propulsion is generated from the electroosmosis created by catalytic reaction [14], the microjet is essentially propelled via bubble created by catalysis. In [9] the authors have identified the jet-internal phenomenon that induces the propulsion of the microjet. This work also proposed to model and to quantify the propulsion of the jet, via the partial transfer of quantity of momentum between the microjet and the moving liquid at both orifices. In the same way, in [15] are proposed a set of one-dimensional reaction diffusion equations to describe the mass transport and reaction in cylindrical microjet to predict the H_2O_2 consumption rate, O_2 bubble growth, and transport. Nevertheless, it is necessary to properly model the microjet propulsion to ensure the proper execution of future missions. This includes the study of the influence of the geometry and confined environment of the microjet. In particular, Sanchez *et al.* have first demonstrated that microjets are able to move efficiently in microfluidic channel even against the flow stream [16]. For instance, the dependence of the performance of the jet wrt. its own geometry is presented in [7] and a unified model is proposed in [17]. In [7], [8] the authors have studied the influence of the chemical environment on its performance. These works show that the microjet can reach speeds of around 1 mm/s, which is well above the speed of $100 \mu\text{m/s}$ raised in [9]. In [8] the authors warn against chemical catalysis brakes, both for its successful implementation and for its influence on propelling the microjet. The geometry of its environment (including the radius of the microchannel) also influences the performance of the microjet, which remains to be studied.

To improve the understanding of the propulsion of the catalytic tubular microjet in confined environment, it is still necessary to consider the following points. Firstly, the motion of the surrounding liquid has to be related to the thrust mechanism. This allows its systemic study and integration to the understanding of the movements of group of microjets and the interaction – through the liquid – with any other objects in the surrounding environment, such as blood cells, bacteria, and so on. Secondly, the various aqueous force

B. Sarkis is with Université Pierre et Marie Curie - Paris 6, France.

D. Folio and A. Ferreira are with INSA Centre Val de Loire, Université d'Orléans, PRISME EA 4229, Bourges, France. Corresponding author: antoine.ferreira@insa-cvl.fr

fields which help propelling the microjet have to be identified and distinguished through Stokes equations, for the future control of its motion. Thirdly, it should be understood how the geometry of surrounding environment (here, the microfluidic channel) influences the microjet propulsion. This allows selecting the most relevant biomedical applications framework, and compensating any physicochemical barriers to the propulsion.

This article aims to address these issues through a qualitative analysis by simplified analytical calculation of the Poiseuille flow driven by the stationary Stokes equations, in the case of a cylindrical microjet navigating on the centerline of a slender cylinder filled with liquid. This paper extends results that first appeared in [18], as well as additional formal designs for novel confined applications. Especially, this study will focus on the use of catalytic microjet for future biomedical applications through the microvascular system [19]. **But, other confined environment could be envisaged.** The proposed analytical framework provides a simple understanding of how the "jet-liquid-wall" system parameters help and influence the propulsion of the microjet **in confined media**. Furthermore, comparison with experimental results that confirm the theory contained herein is presented and discussed.

This paper is organized as follows. After describing the context of our study in Section II, Section III presents a modeling of the microjet in microchannel. The influence of the radius of the vessel on the geometry of flow (and thus the velocity gradients, pressures, shear and microjet propulsion), is studied in Section IV. Finally, Section V discusses the results and some open issues. This study is concluded in Section VI.

II. PROBLEM FORMULATION

Among proposed microsystems, catalytic tubular microjets are the promising microtool for future biomedical applications, as they are self-propelled and do not require any supply of energy except for their guidance [1], [2]. Particularly, it is established that such microsystem can be used in innovative minimally invasive surgical procedures [1], [2], [19]. When the microjets are propelled in the blood circulatory system, a very large number of remote locations in the human body become accessible. However, the human vascular network hemodynamics changes with the vessel radius [19]: from arteries with a large radius of about $R_c = 10$ mm, a viscosity of $\eta = 3$ mPas and a mean flow velocity of $v_f = 400$ mm/s; to capillaries with small radius down to $R_c = 10$ μ m, a viscosity of $\eta = 6.5$ mPas and a flow less than $v_f \leq 1$ mm/s [20]. It is still challenging driving suitably such wireless microdevices in the human cardiovascular system [19]. Improving the understanding of the interaction of these microsystems in a vascular like environment is an important issue.

A. The Microjet

Classically, tubular microjets are manufactured by mainly to two techniques: rolling-up a bimetallic sheet or template-based electrodeposition [4], [5], [8], [9], [21]. The shape of the microjets are a quasi-cylindrical hollow truncated cones, as depicted in Fig. 1 and 2. The basic propulsion principle of the microjet is as follows: gas is produced by catalysis,

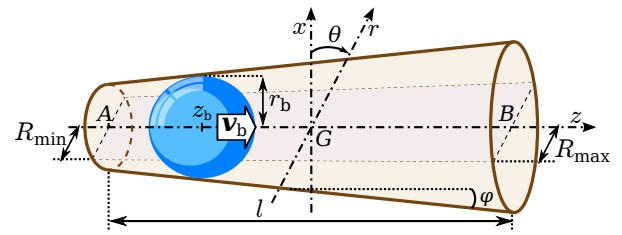


Fig. 1. Schematic representation of a microjet and its bubble.

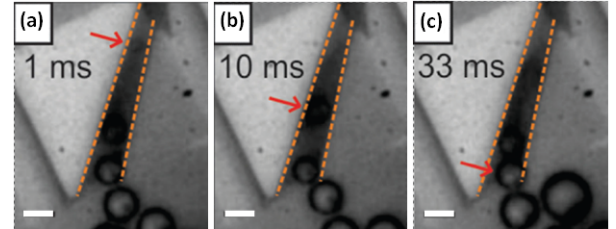


Fig. 2. Generation of an O_2 bubble inside of the tube in an aqueous solution of 1% H_2O_2 and 1% SDS. (a) Inner surface of Pt catalyzes the decomposition of H_2O_2 fuel, and consequently, the generation of an O_2 bubble. (b) Bubble growth and movement to the larger opening of the tube. (c) Bubble is released. The orange dashed lines highlight the walls of the rolled-up tube. The red arrow shows the evolution of a single bubble inside of the tube. Scale bar 10 μ m. (Courtesy of Leibniz Institute for Solid State and Materials Research Dresden [9])

and rapidly forms one (or several) bubble(s) (Fig. 2a). The bubble migrates towards the widest opening of the jet, and propels it towards the opposite direction (Fig. 2b). Finally, the bubbles are released from the tube which induces another moving step (Fig. 2c). If the phenomenon is qualitatively identified, to date we do not know the quantitative influence of the channel geometry on the microjet motion, **especially in confined environment**. To understand this impact, it is necessary to analyze the jet-bubble-liquid-wall interactions. Actually, the flow generates both the propulsion and the brakes of the microjet by its pressure on the bubble and through the shear stress exerted on its inner and outer walls. To quantify these motor and brake, the flow around the microjet should be first characterized. In the reference frame of the microjet which navigates at speed v_j in the channel, Fig. 3 represents the flow around the microjet as the superposition of two components: i) the driving flow, due to the migration of the bubble at speed v_b toward the rear of the microjet; and ii) the drag flow, caused by the recoil velocity of the channel relatively to the microjet. Due to the migration of the bubble, the driving flow induces an overpressure at the rear of the microjet. In addition, the incompressibility of the flow implies an external backflow around the jet outer wall. These two phenomena tend to propel the microjet. Nevertheless, an induced internal wall shear stress occurs and leads to a brake that pulls back the microjet. Their superposition and impact on the microjet (force and speed) are presented in the following sections.

B. The Bubble

At t_0 gas is produced by catalysis at a random nucleation site inside the microjet, and rapidly forms a bubble. **During this growing stage, the microjet is not in contact with the**

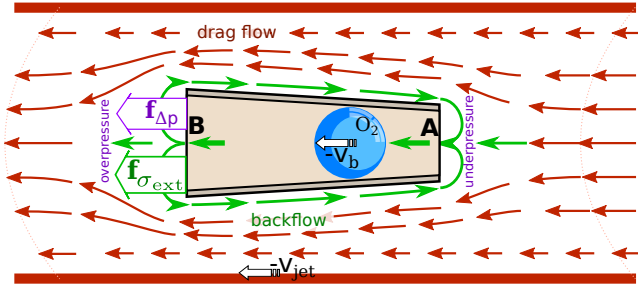


Fig. 3. Flow structure around a microjet, viewed in its reference frame. Flow is the superposition of two components: (green) the migration of the bubble propelling the microjet; (red) the consequence of the motion of the microjet that tends to drag it. Relatively to the microjet, the microfluidic channel moves at speed $-v_j$, and the bubble at $-v_b$. The two driving forces of the microjet are pressure force, $\mathbf{f}_{\Delta p}$, and shear forces, \mathbf{f}_σ .

bubble and, therefore, does not move. At $t_1 = t_0 + \Delta t_1$ ($\Delta t_1 \approx 1$ ms), the bubble becomes tangent to the jet, begins to migrate to the rear B , and the microjet start to move [9]. The migration speed of the bubble, v_b , mainly depends on its growth rate, nucleation position, and on the geometry of the jet [7], [9], [22], [23]. The bubble is ejected at $t_2 = t_1 + \Delta t_2$ (eg. Δt_2 is ranging from 20 ms to 50 ms) at B with a velocity v_b . When at t_1 the bubble reaches the inner wall of the microjet, it becomes a *microswimmer*, and thus obtains their usual properties. Especially, the distance, L_j , traveled during a stroke is independent of its run time, suggesting a relationship of the type:

$$v_j = \frac{L_j}{\Delta t_1 + \Delta t_2} \propto v_b \quad (1)$$

A key issue is to refine the above qualitative relationship (1) according to the environment in which the microjet navigates.

C. The forces

By migrating the bubble swallows the flow at the front (A) and pushes the liquid at the rear (B). This creates a pressure differential between its two hemispheres, wrt. the pressure p_∞ far from the jet. Let $p_\infty - \Delta p_A$ (with $\Delta p_A > 0$) denotes the pressure at the front, and $p_\infty + \Delta p_B$ (with $\Delta p_B > 0$) denotes the pressure at the rear. Hence, the difference established: $\Delta p = \Delta p_A + \Delta p_B$, exerts a pressure difference force $\mathbf{f}_{\Delta p}$, which is a first engine of the microjet. Secondly, the pressure differential can be decomposed in the microjet inner pressure Δp_{int} , and the external pressure Δp_{ext} :

$$\Delta p = \Delta p_{\text{int}} + \Delta p_{\text{ext}} \quad (2)$$

Moreover, the backflow caused by the external flow creates a shear stress σ_{ext} on the external surface of the microjet wall. In particular, on the microjet wall the fluid flows in the opposite direction of the bubble motion, that is in the microjet forward direction. Therefore, the resulting force $\mathbf{f}_{\sigma_{\text{ext}}}$ also contributes to the microjet propulsion. Due to the internal fluid approximative balance through a very weak instantaneous variation of momentum (whose order of magnitude is 10^{-14} N, while that of the propulsion force is 10^{-10} N [9]), the internal

pressure force $\mathbf{f}_{\Delta p_{\text{int}}}$ is compensated by the force $\mathbf{f}_{\sigma_{\text{int}}}$ which is related to the internal shear stress σ_{int} , that is:

$$\mathbf{f}_{\Delta p_{\text{int}}} + \mathbf{f}_{\sigma_{\text{int}}} = 0 \quad (3)$$

Thus, the thrust of the jet is mainly given by the external forces:

$$\mathbf{f}_j \equiv \mathbf{f}_{\Delta p_{\text{ext}}} + \mathbf{f}_{\sigma_{\text{ext}}} \quad (4)$$

Then, at equilibrium, the propulsion of the jet is counteracted by its drag force:

$$\mathbf{f}_j = -\mathbf{f}_d \quad (5)$$

The microjet propelling force \mathbf{f}_j through the drag force \mathbf{f}_d has been first considered as being linked to the microjet velocity v_j by [22], [24]:

$$\mathbf{f}_j = \frac{2\pi \eta l}{\ln(l/R_j) + c_1} v_j \quad (6)$$

with η the dynamic viscosity of the flow, and c_1 depends on the shape of the micromotor. For instance, when the microjet geometry is assumed cylindrical its value is $c_1 = -0.72$ [9]. Li *et al.* [22] propose a solution for conical microjet which leads to $c_1 = -0.8048$ with the value given in Table I. An alternative calculation, will be carried out in the following as comparative perspective.

D. Assumptions

To simplify the analytical description of the microjet functioning, in the following, it is considered as cylindrical microtube of radius R_j and length l , as illustrated in Fig. 4. On the one hand, inside the microjet, this cylindrical approximation is neither relevant nor necessary to analyze the fluid dynamics: thanks to it balance mentioned in II-C, we are allowed not to consider this fluid part in our model. On the other hand, outside the microjet (i.e. where we focus), this approximation is both relevant (for a micro capillary 10 times larger than the microjet, the error on the pressure gradient and the speed are roughly estimated at 4×10^{-3} and 2×10^{-2} [9]) and considerably simplifying the calculations. Thus, without claiming that this approximation is very precise and relevant inside the microjet, it nonetheless catches the essential of the propulsion model when it is applied to the external fluid in the backflow zone. The created bubble is assumed to be spherical with a radius equal to the microtube radius R_j . This single bubble generates an *influence zone* which is assumed to be cylindrical with length $2R_j$. Outside of this influence area, the microjet inner flow behaves as a Poiseuille flow. **The case of multiple nucleation of bubbles and the overloaded microjet is not considered in the present work.** The microfluidic channel is considered to be a cylindrical pipe of radius R_c with an infinite length ($L \gg R_c$). It is filled with a liquid with viscosity η , and having a laminar flow.

Assuming that the microjet is on the centerline of the microchannel, the forces are coaxial with the jet. We consider that the migration of the bubble mechanically transmits perfectly the pressure forces to the microjet. As mentioned, it can be shown that the internal forces counteract each other, as expressed in Eq. (3). Furthermore, the external differential

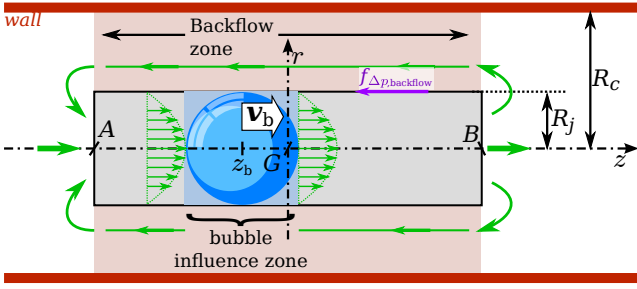


Fig. 4. Representation of the microjet and the inner flow under the simplifying approximations.

pressure Δp_{ext} is considered here only for the backflow region ($\Delta p_{ext, backflow}$), which is assumed to have a linear behavior. Indeed, the inside and the backflow zone of the microjet are only parted by one microjet thickness (e.g. in the order of tens nanometers). Thus, this work assumes that this differential pressure is the one which mainly contribute to the pressure force, that is:

$$f_{\Delta p_{ext}} \approx f_{\Delta p_{ext, backflow}} \quad (7)$$

In the following, we will focus on the backflow located at the upstanding of the jet, which is assumed to be permanent, parallel to the z -axis and independent of z (see Fig.4). The only non-permanent variable is the pressure within the jet.

Finally, the contribution of the overpressure in the bubble is neglected according to its sphericity. Likewise, thermal effects are not addressed in this work. Similarly, the steric, the Brownian, the electrostatic and the Van der Waal's microforces are neglected [25].

E. Numerical Validation

To validate numerically the analytical formulation describing the behavior of a catalytic microjet evolving in a microchannel, a careful three-dimensional (3D) computational fluid dynamics (CFD) modeling has been realized with OpenFOAM[®] (Open Field Operation and Manipulation) toolbox [26]. OpenFOAM is a free, open-source software package that provides solvers for continuum mechanics problem including CFD problem. In particular, the `interFOAM` numerical solver is used here to solve the Stokes equations for an incompressible transient two-phase immiscible fluids by employing the volume-of-fluid (VOF) method. Actually, in our case they are i) the liquid phase that is aqueous solution, and ii) the gas phase. The VOF method determines the relative volume fraction of the two phases in each computational cell, and calculates their physical properties. Specifically, the solver use the multi-dimensional universal limiter for explicit solution (MULES) algorithm for the transport equation, and a merged PISO–SIMPLE¹ algorithms to solve the coupled pressure-velocity fields in large time-step transient domain [26], [27].

¹PIMPLE (merged PISO–SIMPLE) algorithm: Pressure Implicit with Splitting of Operators (PISO) and Semi-Implicit Method for Pressure Linked Equations (SIMPLE) algorithms.

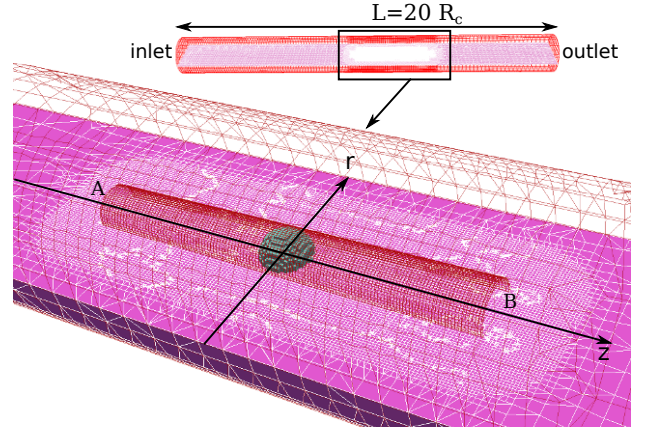


Fig. 5. Illustration of the 3D mesh of a microjet with its bubble (O_2) in a microchannel of radius $R_c = 15 \mu\text{m}$.

1) *3D Computational Domain and Initial Conditions:* To investigate the influence of the microchannel on the microjet behavior, cylindrical pipe with different radii, $R_c \in [6; 60] \mu\text{m}$, and length of $L_c = 20R_c$ have been addressed. First, a conical catalytic microjet has been developed with a CAD software and stored in stereolithography (STL) formatted data. Its main geometrical characteristics is reported in Table I. Secondly, the mesh of the problem are designed with `blockMesh` and the `snappyHexMesh` OpenFoam tools. Furthermore, the OpenFOAM pre-processing tool is employed to define the initial condition of the gas bubble within the microjet, including its velocity v_b . Fig.5 illustrates an example of the simulation domain, that comprises i) the conical microjet; ii) the bubble in its center; and iii) the microchannel here of radius $R_c = 15 \mu\text{m}$ and length $L_c = 300 \mu\text{m}$, filled with a liquid that is composed with aqueous solution. Table II shows the relevant physical properties of the considered fluid and gas.

TABLE I
CONICAL MICROJET AND ITS BUBBLE (SAME AS IN [9]).

Radii	$R_{min} = 3 \mu\text{m} ; R_{max} = 3.5 \mu\text{m}$
Thickness	20 nm
Length	$l = 50 \mu\text{m}$
Bubble	$R_b = 3 \mu\text{m}; v_b = 1.2 \text{ mm/s}$

TABLE II
PHYSICAL PROPERTIES OF THE FLUID AND BUBBLE AT 25 °C.

	Fluid	Gas
Density ρ (kg/m ³)	1000	1.33
Viscosity η (mPa·s)	1.13	20×10^{-3}
Surface tension	0.073 N/m	

At run time $t = 0$, an initial stationary flow is defined through a pressure inlet/outlet velocity boundary condition (BC), and a no-slip BC at the walls of the microchannel and of the microjet. Insofar as the Reynolds number remains low ($Re < 0.07$), all simulations assume a laminar flow behavior. Moreover, the bubble migrates to the rear B of the jet (depicted with the arrow in Fig. 6) with the velocity $v_b = 1.2 \text{ mm/s}$. A variable adjusted time step is defined (initialized with

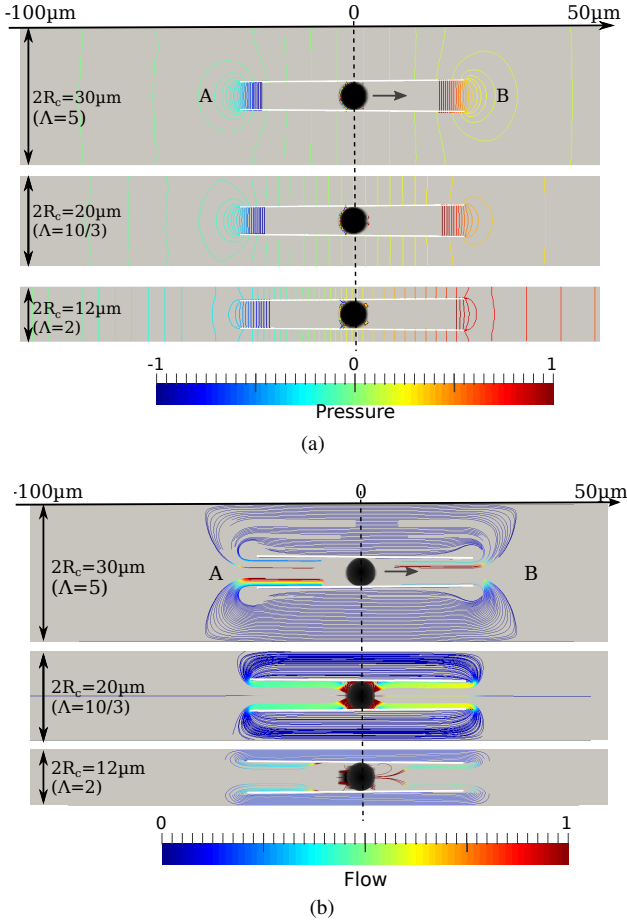


Fig. 6. Numerical simulation results showing at $t = 0.1$ ms: (a) pressure isolines, and (b) the normalized fluid flow streamlines when the bubble (in black) is in the center of the jet in microchannel of radius of: (top) $R_c = 15 \mu\text{m}$, (middle) $R_c = 10 \mu\text{m}$, and (bottom) $R_c = 6 \mu\text{m}$. The arrow depicts the bubble migration direction.

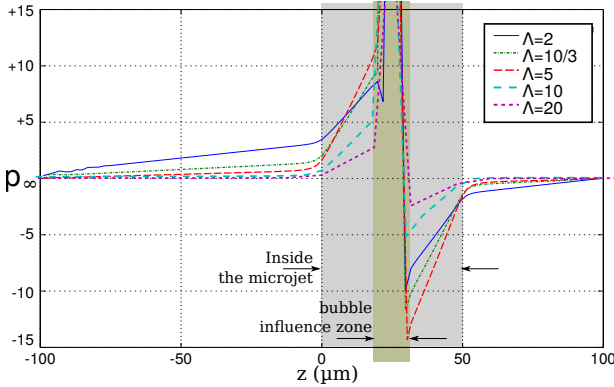


Fig. 7. Pressure along the centerline when the bubble is in the center of the microjet.

$\Delta t = 10$ ns) and does not exceed $\Delta t = 63.5$ ns with a maximum courant number of 0.09. Simulations are carried out until $t = 0.1$ ms. Fig. 6 shows a zoomed view of the microchannel, and some obtained numerical simulation results for a catalytic microjet that navigates in microchannel of radii (top) $R_c = 15 \mu\text{m}$ to (bottom) $R_c = 6 \mu\text{m}$. Fig. 6a illustrates the pressure isolines which have their greatest values inside the

conical microjet hollow, with negative values on the left side of the bubble and positive values on its right side. Fig. 6b shows the normalized fluid flow streamlines which remain globally parallel at the upstanding of the microjet. **These results are in accordance with the numerical modeling achieved in [28].**

2) *Assumptions Validation*: A main key issue of the proposed mathematical model rely on the differential pressure assumption that leads to the relation (7). Indeed, the external differential pressure is well defined mainly for the backflow region (cf. Fig. 4). In this domain, the pressure and the velocity are considered to behave linearly. When the bubble is in the middle of the microjet, the Fig. 6a illustrates the pressure isolines for microchannel of radius ranging from $R_c \in [6; 15] \mu\text{m}$. For small radii ratio $\Lambda = R_c/R_j$, the assumption appears clearly in good agreement with the numerical results. A decrease of the validity region occurs while Λ is growing. The pressure along the axial z -axis (i.e. for $r = 0$), when the bubble is in the center of the jet, is shown in Fig. 7. As expected, it appears a discontinuity in the bubble influence area. Actually, the pressure is not defined when $\forall z \in]-R_j; R_j[$. When the bubble moves back, the discontinuity shifts toward the rear B of the jet. Let us notice that the pressure has a linear behavior inside the jet. The external pressure differential Δp_{ext} remains constant when the bubble moves inside the microjet. The computed numerical simulation results validate the formulated qualitative assessment.

III. GENERALIZED MATHEMATICAL MODEL

A. Theoretical Foundation

Considering the previous assumptions, the microjet propulsion involves mainly the surrounding flow. Hence, the Stokes equations together with the flow incompressibility allow the modeling of the microjet's engines. Moreover, with the assumption of no tangential velocity the considered system is here axisymmetric (see Fig. 4). In this context, the incompressible Stokes equations in cylindrical coordinates is then basically considered:

$$\eta \left(\frac{1}{r} \partial_r (r \partial_r v_r) + \partial_z^2 v_r - \frac{v_r}{r^2} \right) = \partial_r p \quad (8)$$

$$\eta \left(\frac{1}{r} \partial_r (r \partial_r v_z) + \partial_z^2 v_z \right) = \partial_z p \quad (9)$$

$$\frac{1}{r} \partial_r (r v_r) + \partial_z v_z = 0 \quad (10)$$

with $r \in [0; R_c]$ the radial distance; z the axial component; the velocity vector expanded here in cylindrical coordinates as $\mathbf{v} = (v_r, v_z, 0)^t$; and ∂_r denotes the partial derivative wrt. r . In the following the hydrodynamics and propulsion mechanism of the microjet in its reference frame is investigated.

The fluid around the microjet induces obviously an internal drag, but also a thrust on it thanks to the shear stress σ_{ext} in the backflow area. Hence, the liquid exerts a force \mathbf{f}_a that is related to the engine flow \mathbf{f}_j or to the drag flow \mathbf{f}_d . Each of these partial flows forces is divided into two strain forces on the microjet: a pressure force $\mathbf{f}_{\Delta p_a}$, and a shear stress force \mathbf{f}_{σ_a} , as in (4). In the case of the engine flow, it is respectively $\mathbf{f}_{\Delta p_a} \equiv \mathbf{f}_{\Delta p_{\text{ext}}}$ and $\mathbf{f}_{\sigma_a} \equiv \mathbf{f}_{\sigma_{\text{ext}}}$. Whereas, considering the drag flow we get respectively $\mathbf{f}_{\Delta p_a} \equiv \mathbf{f}_{\Delta p_d}$ and $\mathbf{f}_{\sigma_a} \equiv \mathbf{f}_{\sigma_d}$.

1) *Generalized Flow Field and Pressure Gradient*: Let us recall that only the pressure differential Δp_{ext} in the backflow region is considered here. Therefore, the previous Stokes equations (8)-(10) could be expressed as:

$$\exists \lambda_a > 0 \quad \left\{ \begin{array}{l} -\partial_z p \equiv \lambda_a = \Delta p_a / l \\ \partial_r (r \partial_r v_z) = -\lambda \frac{r}{\eta} \\ (\partial_r p, \partial_z^2 p)^t = (0, 0)^t \end{array} \right. \quad (11)$$

Secondly, each pressure differential Δp_a in the backflow zone is associated with a uniform pressure gradient defined as:

$$\lambda_a \equiv -\Delta p_a / l \quad (12)$$

As previously, in the case of the engine flow we get $\lambda_a = \lambda_j$, and for the drag flow $\lambda_a = \lambda_d$. Let us notice that, according to the linearity of the Stokes system, these boundary considerations can be applied to the real flow, which is the superposition of the motor flow and the drag flow.

As mentioned, the microjet frame \mathcal{F}_j is considered as the reference frame. For each partial flow, let Q_a be the algebraic flow rate toward the z -axis across any section of the backflow zone orthogonally to z . Let $v_{0,a}$ defines the motion of the microchannel wall in \mathcal{F}_j , and $v_{z,a}$ the z -axial component of the velocity field created in the backflow zone. Then, the Stokes (11) goes with the following BC:

$$\left\{ \begin{array}{l} v_{z,a}(r = R_j) = 0 \\ v_{z,a}(r = R_c) = v_{0,a} \\ \int_{R_j}^{R_c} 2\pi r v_{z,a}(r) dr = Q_a \end{array} \right. \quad (13)$$

The general expression of the velocity $v_{z,a}$ bound to the action of each partial flow is expressed by integrating the Stokes equations (11) two times with the above BC (13), and we get:

$$v_{z,a}(r) = \frac{\lambda_a R_j^2}{4\eta} \left((\Lambda^2 - 1) \frac{\ln(r/R_j)}{\ln \Lambda} + 1 - \left(\frac{r}{R_j} \right)^2 \right) + v_{0,a} \frac{\ln(r/R_j)}{\ln \Lambda} \quad (14)$$

with $\Lambda = R_c/R_j$ radii ratio.

In the upstream and downstream of the microjet, it is difficult to fully analytically characterize the driving flow. However, its velocity norm remains less than the bubble speed v_b . In the backflow zone, let v_{max} denotes the maximum motive speed, and $r_{\text{max}} \in [R_j; R_c]$ defined such as $v_z(r_{\text{max}}) = v_{\text{max}}$. A dimensional analysis shows that Δp_{ext} is in the order of: $\Delta p_{\text{ext}} \approx 2\eta \frac{v_{\text{max}}}{r_{\text{max}}}$.

The computation of the backflow pressure gradient λ_a is then performed by writing the flow conservation between the flow inside the microjet and the backflow area, leading to:

$$\lambda_a = \frac{4\eta}{R_j^2} \frac{\frac{2Q_a}{\pi R_j^2} \ln(\Lambda) - v_{0,a} (2\Lambda^2 \ln(\Lambda) + 1 - \Lambda^2)}{(\Lambda^2 - 1) ((\Lambda^2 + 1) \ln(\Lambda) + 1 - \Lambda^2)} \quad (15)$$

2) *Generalized Forces*: The pressure force $\mathbf{f}_{\Delta p_a}$ exerted on a cylindrical microjet is here bound to the pressure difference $\Delta p_a = -\lambda_a l$, and could be expressed as:

$$\mathbf{f}_{\Delta p_a} = \pi R_j^2 l \lambda_a \quad (16)$$

The shear stress force is basically defined as:

$$\mathbf{f}_{\sigma_a} = 2\pi l R_j \sigma_a \quad (17)$$

where the shear stress is computed from:

$$\sigma_a = \eta \partial_r v_z |_{r=R_j} \quad (18)$$

By derivating the Eq. (14) and then replacing Λ_a by its value given by (15) we get:

$$\sigma_a = \frac{1}{R_j} \left(\frac{\lambda_a R_j^2}{4} \left(\frac{\Lambda^2 - 1}{\ln(\Lambda)} - 2 \right) + \frac{\eta v_{0,a}}{\ln(\Lambda)} \right) \quad (19)$$

Finally, the total strain force exerted on the microjet by the partial flow is obtained by summing (16) and (17), that is:

$$\mathbf{f}_a = \mathbf{f}_{\Delta p_a} + \mathbf{f}_{\sigma_a} = 2\pi \eta l \frac{2 \frac{Q_a}{\pi R_j^2} + v_{0,a} (1 - \Lambda^2)}{(1 + \Lambda^2) \ln(\Lambda) + 1 - \Lambda^2} \quad (20)$$

IV. OPTIMIZATION FOR NAVIGATION IN CONFINED ENVIRONMENT

The obtained mathematical model (20) describes the driving flow and drag flow interactions on the microjet. This paragraph shows how to apply this result to retrieve the different contributions.

A. Static fluid flow

The following is devoted to the study of the microjet interaction with each partial flows in its own reference frame \mathcal{F}_j , first considering a static flow for the sake of simplicity.

1) *The Microjet Engine*: To determine the thrust of the jet \mathbf{f}_j , the microjet is considered static even though its motor flux is in action. Secondly, the flow rate Q_j of the driving flow corresponds to the one inside the microjet due to the bubble migration with a velocity v_b . This leads to the following specific BC of the engine flow:

$$\left\{ \begin{array}{l} v_{0,a} \equiv v_{0,j} = 0 \\ Q_a \equiv Q_j = \pi R_j^2 v_b \end{array} \right. \quad (21)$$

Thus, by apply this boundary conditions to (15) the driving pressure gradient is basically expressed as:

$$\lambda_j = \frac{8\eta}{R_j^2} \frac{\ln(\Lambda) v_b}{(\Lambda^2 - 1) ((\Lambda^2 + 1) \ln(\Lambda) + 1 - \Lambda^2)} \quad (22)$$

The pressure and shear stress propelling forces is given by:

$$\mathbf{f}_{\Delta p_{\text{ext}}} = \frac{8\pi \eta l \ln(\Lambda) v_b}{(\Lambda^2 - 1) ((\Lambda^2 + 1) \ln(\Lambda) + 1 - \Lambda^2)} \quad (23)$$

$$\mathbf{f}_{\sigma_{\text{ext}}} = \frac{4\pi \eta l (\Lambda^2 - 1 - 2 \ln(\Lambda)) v_b}{(\Lambda^2 - 1) ((\Lambda^2 + 1) \ln(\Lambda) + 1 - \Lambda^2)} \quad (24)$$

Finally, the microjet thrust force is deduced by applying (20):

$$\mathbf{f}_j = \frac{4\pi \eta l v_b}{(\Lambda^2 + 1) \ln(\Lambda) + 1 - \Lambda^2} \quad (25)$$

2) *The Drag Flow*: In the microjet reference frame \mathcal{F}_i , the microchannel wall is moving at $-v_j$. Hence, the drag flow rate Q_d is related to the microjet motion, and the following BC have to be considered:

$$\begin{cases} v_{0,a} \equiv v_{0,d} = -v_j \\ Q_a \equiv Q_d = -\pi R_c^2 v_j \end{cases} \quad (26)$$

As previously, by applying (20) we get:

$$f_d = -\frac{2\pi l \eta (1 + \Lambda^2) v_j}{(1 + \Lambda^2) \ln(\Lambda) + 1 - \Lambda^2} \quad (27)$$

3) *The Microjet Velocity*: Using (27) with (25), it is straightforward to obtain a simple formula that relates the velocities v_j and v_b by considering the equilibrium condition (5), and we get:

$$v_j = \frac{2v_b}{1 + \Lambda^2} \quad (28)$$

Using the same reasoning, one can easily compute the jet velocity using the drag force expression proposed in [9], [22]. Combining Eq. (6) and (25), the relationship (1) can be specified as:

$$v_j = \frac{2(\ln(l/r) + c_1)}{(1 + \Lambda^2) \ln(\Lambda) + 1 - \Lambda^2} \cdot v_b \quad (29)$$

As one can see, it appears that v_j is independent of the liquid's viscosity η , and is mainly related to the geometry of the jet and the channel's size. Thus, the jet presents some scale invariance. Furthermore, the smaller the ratio Λ is, the higher is the velocity of the microjet.

B. Steady fluid flow

The previous results are established considering a globally static liquid. We now consider a more generic case where the global passive flow rate can be non zero in the reference frame of the microchannel. Let Q_f be this flow rate and let $v_f = Q_f/(\pi R_c^2)$ be the corresponding medium speed. Finally, let $Q_d = Q_f - Q_j = \pi R_c^2(v_f - v_j)$ be the global passive flow rate in the reference frame of the microjet. Obviously, the intrinsic microjet engine f_j given by (25) does not change, and only the drag force f_d expression has to be investigated. Then, the two specific boundary conditions of the drag flow become here:

$$\begin{cases} v_{0,a} \equiv v_{0,d} = -v_j \\ Q_a \equiv Q_d = \pi R_c^2(v_f - v_j) \end{cases} \quad (30)$$

As previously, the drag pressure gradient opposite is then deduced from (15) as:

$$\lambda_d = \frac{4\eta}{R_j^2} \frac{2\Lambda^2 \ln(\Lambda)v_f + (1 - \Lambda^2)v_j}{(\Lambda^2 - 1)((\Lambda^2 + 1) \ln(\Lambda) + 1 - \Lambda^2)} \quad (31)$$

and the drag force f_d is basically obtained from (20):

$$f_d = 2\pi \eta l \frac{2\Lambda^2 v_f - v_j(\Lambda^2 + 1)}{(1 + \Lambda^2) \ln(\Lambda) + 1 - \Lambda^2} \quad (32)$$

At equilibrium, f_j is compensated by f_d . Then, the microjet's speed is :

$$v_j = 2 \frac{v_b + \Lambda^2 v_f}{1 + \Lambda^2} \quad (33)$$

This result shows that the jet could swim against the flow so long as $v_f \geq -v_b/\Lambda^2$. Moreover, in large channels, where $\Lambda \gg 1$, we get $v_j \approx 2v_f$, meaning that the microjet is mainly driven by the blood flow.

C. The microjet's bubble detachment

The proposed modeling of the catalytic tubular microjet address its velocity v_j when the bubble migrate towards the largest opening. During motion of the microjet, it is observed that the bubble grown at one end of the microjet, and is released. In quasi-steady state, the current one-dimensional transport model cannot predict the behavior of the bubble after it reaches its maximum size and leaves the end of the microjet (ejection). To model the release of the bubble, Li *et al.* [7] relates the average velocity of the microjet to the frequency of the ejection and the displacement of the microjet in one step. As this model only consider a cylindrical shape, in [22] the authors extends the proposed idea to conical microjets, and suggests the following microjet velocity for the bubble release:

$$v_j^{\text{eject}} = \frac{9nC_{\text{fuel}}l(R_j - \frac{1}{2}\tan\delta)\left(\ln\frac{l}{R_j} + c_1\right)}{3R_b^2\left(\ln\frac{l}{R_j} + c_1\right)\cos\delta + lR_b\cos\delta} \quad (34)$$

with δ the conical angle, n a rate constant and C_{fuel} the concentration of fuel reactant. It can be noticed that the above expression of the microjet velocity does not take into account the channel geometry.

V. RESULTS AND DISCUSSIONS

A. Biomedical application

In this section, we investigate the consistency of the proposed modeling of the catalytic microjet wrt. results reported in the literature. Specifically, the considered microjet is intended for future biomedical application through the vascular system. Despite the significant and fast advances in the field, challenges still remain, especially, to find relevant biologically compatible fuels. Hydrogen peroxide (H_2O_2) is the most utilized fuel for microjet, although its cytotoxicity impedes its application in a biomedical context. Recently, zinc-based motors have been reported for *in vivo* use, particularly for gastric drug delivery, because of their unique features, including acid-powered propulsion, high loading capacity, autonomous release of payloads, and nontoxic self-destruction [29]. In biological blood medium, the authors in [30] reported that at low concentrations of H_2O_2 , and at physiological temperatures, catalytic microjets could move for a short period of time (about 30 min) before the red blood cells (RBCs) undergo apoptosis. To overcome this issue, a solution is to consider non-toxic fuels by the integration of enzymes as active catalyst (catalase, urease and glucose oxidase) [10]. As example, researchers in [31] immobilized catalase into roll-up microtubes providing efficient bubble propulsion (about 10 times faster propulsion than with Pt catalyst) by triggering the decomposition of H_2O_2 inside the microjets. Based on these promising results, we simulated in the following section, the predictable performances of these microjets for future drug delivery applications. To do so, we considered microjets

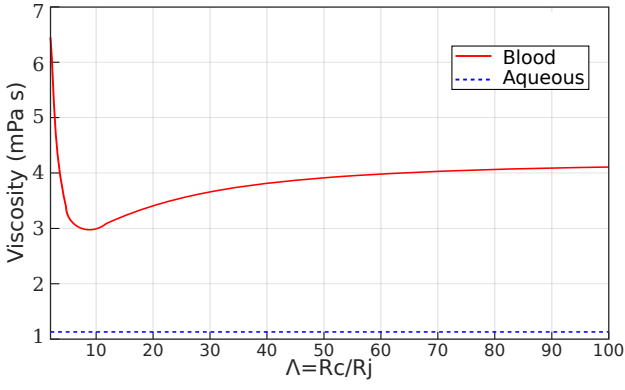


Fig. 8. The blood flow viscosity η as function of $\Lambda = R_c/R_j$.

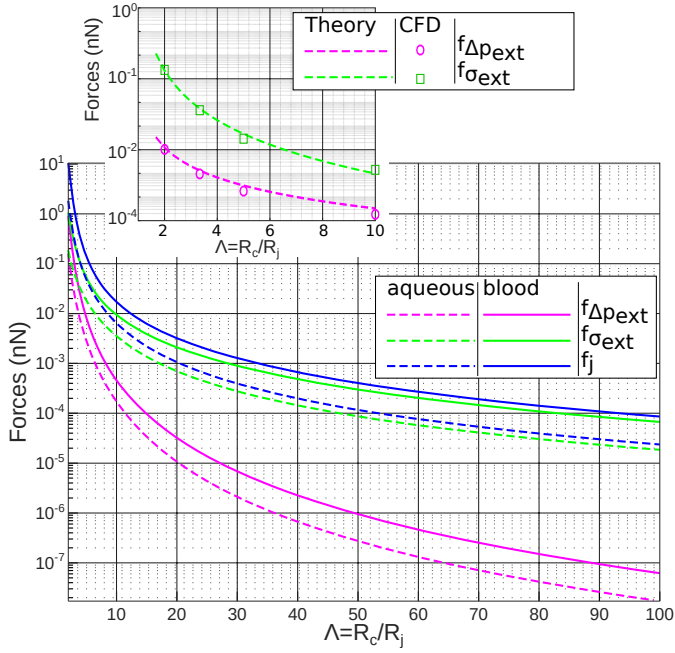


Fig. 9. Representation of f_j , $f_{\Delta p_{ext}}$ and $f_{\sigma_{ext}}$, for $l = 50 \mu\text{m}$ and $v_b = 1.2 \text{ mm/s}$ in blood (see Fig. 8) and aqueous solution ($\eta = 1.13 \text{ mPa s}$ [9]) in capillaries. The inset shows a comparison of the pressure, $f_{\Delta p_{ext}}$ and viscous, $f_{\sigma_{ext}}$, forces over the microjet using analytical model (23)-(24) and the numerical CFD analysis.

navigating in vessel-like microfluidic channels mimicking the anatomical arterial network. For validation purposes, we compared our results to two different types of catalytic microjets (i) the microjet #A issued from [9] and (ii) the microjet #B issued from [12].

B. Static flow model analysis

This section focus on the model analysis without flow velocity. The propelling forces f_j , $f_{\Delta p_{ext}}$ and $f_{\sigma_{ext}}$ are related to the flow viscosity which is considered constant in aqueous solution $\eta = 1.13 \text{ mPa s}$ [9]. In the case of the cardiovascular system, the fluid's viscosity depends mainly on the radius of the vessel [20]. Fig. 8 shows the evolution of the blood flow viscosity for vessels with a radius in the the range of $R_c \in [6; 300] \mu\text{m}$ considering the model proposed by Priest *et al.* [20]. Obviously, as shown in Fig. 9, the propelling forces

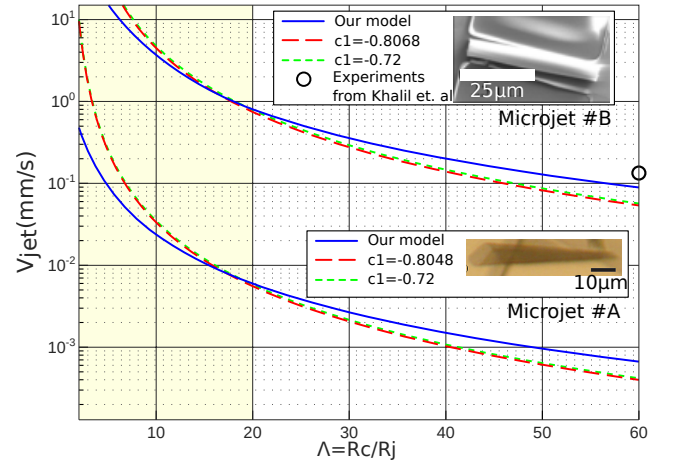


Fig. 10. Velocity v_j for two catalytic microjets: #A same as in [9] and #B same as in [12]. The inlet pictures illustrate these two microjets. The velocity is computed from our proposed formalism (28), and from Eq. (29) considering the cylindrical approximation ($c_1 = -0.72$) and the conical shape ($c_1 = -0.8048$ and $c_1 = -0.8068$). The circle mark show the experimental value from Khalil *et al.* [12].

are more significant in small capillaries where the blood flow viscosity is classically in the range of $\eta \in [2.9; 6.5] \text{ mPa s}$ against aqueous solution with a $\eta = 1.13 \text{ mPa s}$ [9]. These results are in accordance with [30]. Due to the increase of viscosity after the addition of RBC in serum media, the absolute average speed at physiological temperatures ranging from 25°C to 37°C decreased, reaching values from $15 \mu\text{m/s}$ to $25 \mu\text{m/s}$. The authors found that when the viscosity of the solution is higher than $\eta = 1.1 \text{ mPa s}$, microjets cannot self-propel. Secondly, in smaller channel (e.g. in capillaries) the backflow force $f_{\sigma_{ext}}$ and the pressure force $f_{\Delta p_{ext}}$, are maximum, and remain in the same order of magnitude. In large channels $f_{\sigma_{ext}}$ is more significant than $f_{\Delta p_{ext}}$, but these two driving forces are clearly weakening, as illustrated in Fig. 9. Let us recall that the proposed formalism remains mainly valid for confined microfluidic channels. Finally, the inset in Fig. 9 shows that the analytical model fit suitably the calculated forces from CFD results presented in Section II-E.

For a bubble motion at $v_b = 1.2 \text{ mm/s}$ the microjet velocity remains $v_j \leq 1.2 \text{ mm/s}$, as represented in Fig. 10 with the microjet #A issued from [9]. This result is consistent with previous studies [7]–[9], [12], [32]. Particularly, a maximal jet velocity of about $v_j \approx 1.5 \text{ mm/s}$ has been reported [7], [32]. On the other hand, the impact of the drag pressure is more significant in capillaries, but is negligible in larger vessels. The catalytic microjet #B shown in Fig. 10 [12] was propelled inside a microchannel with time varying flow rates (cf. Section V-C). The circle mark shows an experimental value extracted from [12] when there is no flow in the microfluidic channel. Although the assumptions of our model are mainly valid in small microfluidic channels (e.g below $\Lambda < 20$), it appears that the proposed formalism is able to suitably predict the motion of the microjet in static flow.

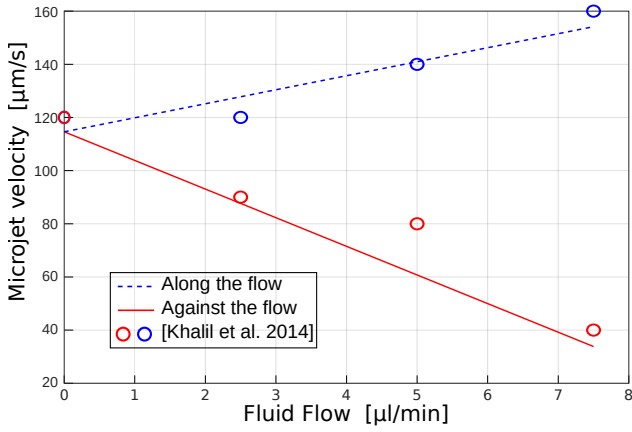


Fig. 11. Average velocity of the microjets against and along flow rates. Comparison between simulation results (solid and dashed lines) and experiments (circle marks) extracted from the works of Khalil *et al.* [12]. The velocity of the microjet decreases and increases when microjets move against (red) and along (blue) the controlled flow in the microchannel.

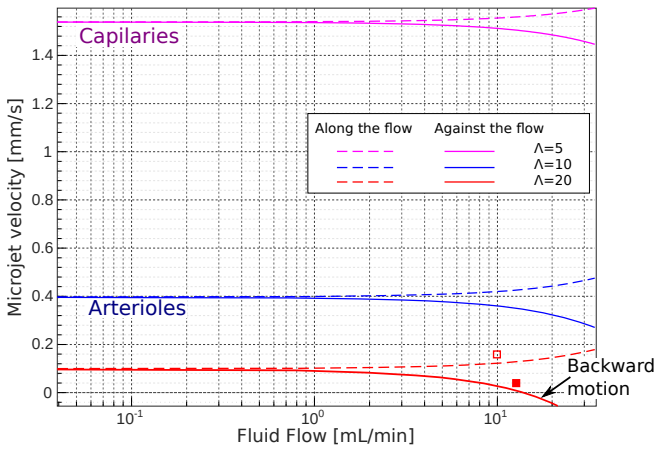


Fig. 12. Evaluation of the microjet velocity as function of the fluid flow for different microfluidic channel sizes mimicking capillaries and arterioles. The square markers refer to experimental values extracted from [16] for against (filled square) and along the flow (red box).

C. Fluid flow model analysis

In this section, we evaluate the consistency of the proposed modeling when considering fluid flow dynamics. The authors in [12] have conducted some experiments with a catalytic microjet navigating inside a microfluidic channel at flow rates ranging from 0 $\mu\text{l}/\text{min}$ to 7.5 $\mu\text{l}/\text{min}$. The microchannel is similar to the sizing of small arteries. The experimental results are reported in Fig. 11 (circle marks), together with our proposed modeling applied to the microjet #B extrapolated from the one presented in [12]. As one can see, the formulated methodology predicts suitably the behavior of the microjet along and against the fluid flow wrt. the reported experimental data. Actually, the fluid flow impacts not only the microjet motion but the bubble motion too. It should be noticed that the velocity of the bubble decreases when the microjet moves along the flow and increases when the microjet moves against the flow (bubble transport and flow in the same direction).

Fig. 12 illustrates the microjet velocity as function of the fluid flow for arterioles and capillaries. As expected in previ-

ous calculations, the microjet velocity is increasing with the decreasing of the vessel's size. It can be noticed that in large vasculature, the microjet cannot counteract the fluid flow and is carried away by the flow. The performance analysis shows that the microjet seems to be an ideal candidate to navigate into capillaries but in other hand, appears less efficient in large vessels where the fluid flow is too strong. These findings are in accordance with the experiments conducted in [16], [33]. In [33] CaCO_3 particles were capable of transporting upstream against blood flow through a glass capillary at velocities between 0.06 mm/s and 5.9 mm/s but likely not against blood flowing through arteries. A slight discrepancy could be observed with the experimental results conducted in [16] (square markers in Fig. 12). This exhibits the limit of the presented model for $\Lambda > 20$.

D. Discussion

Biocompatible tubular microjets hold great potential for active drug delivery in vitro (microfluidic lab-on-chips) and even in vivo (small animal assays). The simulation results presented here aim to predict their performances in such environments. The proposed microjet propulsion model is simple under the considered assumptions. The associated calculations are conducted thanks to approximations of the Stokes equations, which can be gathered into three groups: i) geometrical and mechanical aspects that concern mainly the walls of the microjet and the vessel; ii) fluid flow dynamics surrounding the jet propulsion; and iii) force approximations, which involve their orientations and the link between the drag force and the velocity of the microjet. For instance Eq.(28) matches suitably the numerical and experimental results presented in [7]–[9], [12], [32]. Especially, the increase of the velocity in narrow microfluidic channel have been recently observed for bimetallic nanorod [28] with $\Lambda = 4$, validating our proposal. Contrary, in [34] the authors have observed a decrease of the velocity of the nanorod in wide microchannel with $\Lambda > 20$. The raised hypothesis was related to the possible absorption of the stationary fuel into the PDMS channel. To overcome this issue, in [16] a flow is used to set in motion the fuel, increasing the power efficiency for cargo towing. Some hypothesis could be further investigated, such as the bubble's sphericity, or its mechanical contact with the jet wall and its growing speed, as suggested in [9]. The geometry flow of the microjet has to be considered in relation to the study realized in [32]. As example, the authors in [11], [14] have shown that the microjet has a natural deflection similar to nanorod structures. Secondly, in this work only a single bubble is considered in the problem formulation. Further investigations have to be conducted to address multiple bubble nucleation and microjet overloading [23]. Khalil *et al.* have observed in microfluidic channels that bubbles are trapped and their diffusion rate is lower than the diffusion rate inside a petri dish [12]. The interactions forces with several bubbles should significantly influence the catalytic microjet dynamics. A first attempt has been proposed by the authors where the H_2O_2 bubbles were modeled as oblate spheroids (not reported here). It improved the prediction results of Fig. 11 against the static

flow. However, the model does not describe many important aspects of the behavior of microjets in flowing solutions (e.g. turbulent or pulsating flow) or in heterogeneous solutions (e.g. RBCs in blood flow). These aspects will be investigated in a future study.

VI. CONCLUSION

Recently, using catalytic chemical reactions to propel microrobots has attracted a great deal of attention by the robotics community notably in biomedical applications. They are thin, fast, powerful in small vessels, self-propelled, cheap to produce, weakly deflected and easily remote-controllable. Their operating principle remains not fully understood but the rough calculations performed in this study suggest how efficient these microswimmers are, especially in thin fluidic microchannels. Optimization of the microjet geometries needs a deep understanding of bubble migration along the tubular microjet and bubble ejection. The proposed analytical model, validated by computational fluid dynamics simulations, provides a fundamental explanation of the driving forces acting in bubbles at the origin of the catalytic propulsion. From these findings, the locomotion performances of different microjet tubular geometries (length, radius, shape) and the chemical environment (fuel concentration) have been simulated when moving in a low Reynolds number flow through different microfluidic channel dimensions. The predicted results by the derived model are in good agreement with the experimental results found in the literature for cone-type and rolled-up tubular microjets. Our results provide further understanding on tubular microjets in confined environment, which may have potential biomedical applications.

REFERENCES

- [1] J. Wang and W. Gao, "Nano/microscale motors: biomedical opportunities and challenges," *ACS Nano*, vol. 6, no. 7, pp. 5745–5751, 2012.
- [2] J. Li, B. E.-F. de Ávila, W. Gao, L. Zhang, and J. Wang, "Micro/nanorobots for biomedicine: Delivery, surgery, sensing, and detoxification," *Science Robotics*, vol. 2, no. 4, p. eaam6431, 2017.
- [3] A. A. Solovev, Y. Mei, E. Bermúdez Ureña, G. Huang, and O. G. Schmidt, "Catalytic microtubular jet engines self-propelled by accumulated gas bubbles," *Small*, vol. 5, no. 14, pp. 1688–1692, 2009.
- [4] J. Parmar, D. Vilela, and S. Sanchez, "Tubular microjets: Fabrication, factors affecting the motion and mechanism of propulsion," *Eur. Phys. J. Spec. Top.*, vol. 225, no. 11–12, pp. 2255–2267, 2016.
- [5] Y. Mei, G. Huang, A. A. Solovev, E. B. Urena, I. Mönch, F. Ding, T. Reindl, R. K. Fu, P. K. Chu, and O. G. Schmidt, "Versatile approach for integrative and functionalized tubes by strain engineering of nanomembranes on polymers," *Adv. Materials*, vol. 20, no. 21, pp. 4085–4090, 2008.
- [6] Y. Mei, A. A. Solovev, S. Sanchez, and O. G. Schmidt, "Rolled-up nanotech on polymers: from basic perception to self-propelled catalytic microengines," *Chem. Soc. Rev.*, vol. 40, no. 5, pp. 2109–2119, 2011.
- [7] J. Li, G. Huang, M. Ye, M. Li, R. Liu, and Y. Mei, "Dynamics of catalytic tubular microjet engines: dependence on geometry and chemical environment," *Nanoscale*, vol. 3, no. 12, pp. 5083–5089, 2011.
- [8] G. Zhao, S. Sanchez, O. G. Schmidt, and M. Pumerá, "Poisoning of bubble propelled catalytic micromotors: the chemical environment matters," *Nanoscale*, vol. 5, no. 7, pp. 2909–2914, 2013.
- [9] V. M. Fomin, M. Hippler, V. Magdanz, L. Soler, S. Sanchez, and O. G. Schmidt, "Catalytic microjet engines: propulsion mechanisms and performances," *IEEE Trans. Robot.*, vol. 30, no. 1, pp. 40–48, Feb. 2014.
- [10] P. Schattling, B. Thingholm, and B. Stadler, "Enhanced diffusion of glucose-fueled janus particles," *Chemistry of Materials*, vol. 27, no. 21, pp. 7412–7418, 2015.
- [11] L. Baraban, S. M. Harazim, S. Sanchez, and O. G. Schmidt, "Chemotactic behavior of catalytic motors in microfluidic channels," *Angewandte Chemie*, vol. 125, no. 21, pp. 5662–5666, 2013.
- [12] I. S. Khalil, V. Magdanz, S. Sanchez, O. G. Schmidt, and S. Misra, "The control of self-propelled microjets inside a microchannel with time-varying flow rates," *IEEE Trans. Robot.*, vol. 30, no. 1, pp. 49–58, Feb. 2014.
- [13] S. Sanchez, A. A. Solovev, Y. Mei, and O. G. Schmidt, "Dynamics of biocatalytic microengines mediated by variable friction control," *J. Am. Chem. Soc.*, vol. 132, no. 38, pp. 13 144–13 145, 2010.
- [14] W. F. Paxton, K. C. Kistler, C. C. Olmeda, A. Sen, S. K. St. Angelo, Y. Cao, T. E. Mallouk, P. E. Lammert, and V. H. Crespi, "Catalytic nanomotors: autonomous movement of striped nanorods," *J. of the American Chemical Society*, vol. 126, no. 41, pp. 13 424–13 431, 2004.
- [15] M. Manjare, B. Yang, and Y.-P. Zhao, "Bubble-propelled microjets: model and experiment," *J. Phys. Chem.*, vol. 117, pp. 4657–4665, 2013.
- [16] S. Sanchez, A. A. Solovev, S. M. Harazim, and O. G. Schmidt, "Microbots swimming in the flowing streams of microfluidic channels," *J. Am. Chem. Soc.*, vol. 133, no. 4, pp. 701–703, 2010.
- [17] L. Li, J. Wang, T. Li, W. Song, and G. Zhang, "A unified model of drag force for bubble-propelled catalytic micro/nano-motors with different geometries in low reynolds number flows," *Journal of Applied Physics*, vol. 117, no. 104308, pp. 1–6, 2015.
- [18] B. Sarkis, D. Folio, and A. Ferreira, "Catalytic tubular microjet propulsion model for endovascular navigation," *IEEE Int. Conf. on Robotics and Automation*, p. 35373543, 2015.
- [19] B. J. Nelson, I. K. Kaliakatsos, and J. J. Abbott, "Microrobots for minimally invasive medicine," *Annual Review of Bio.med. Eng.*, vol. 12, no. 1, pp. 55–85, 2010.
- [20] A. Pries, T. Secomb, and P. Gaehtgens, "Biophysical aspects of blood flow in the microvasculature," *Cardiovascular research*, vol. 32, no. 4, pp. 654–667, 1996.
- [21] V. Magdanz, M. Guix, and O. G. Schmidt, "Tubular micromotors: from microjets to spermbots," *Robotics and Biomimetics*, vol. 1, no. 1, pp. 1–10, 2014.
- [22] L. Li, J. Wang, T. Li, W. Song, and G. Zhang, "Hydrodynamics and propulsion mechanism of self-propelled catalytic micromotors: model and experiment," *Soft Matter*, vol. 10, no. 38, pp. 7511–7518, 2014.
- [23] A. Klingner, I. S. Khalil, V. Magdanz, V. M. Fomin, O. G. Schmidt, and S. Misra, "Modeling of unidirectional-overloaded transition in catalytic tubular microjets," *J. of Phys. Chem. C*, 2017.
- [24] R. Cox, "The motion of long slender bodies in a viscous fluid part 1. general theory," *J. Fluid Mech.*, vol. 44, no. 04, pp. 791–810, 1970.
- [25] K. Belharet, D. Folio, and A. Ferreira, "Simulation and planning of a magnetically actuated microrobot navigating in the arteries," *IEEE Trans. Biomed. Eng.*, vol. 60, no. 4, pp. 994–1001, 2013.
- [26] (2017, v2.4.0) OpenFOAM: The open field operation and manipulation (CFD) toolbox, user guide. OpenFOAM Foundation. [Online]. Available: <http://www.openfoam.org>
- [27] T. Chung, *Computational fluid dynamics*. Cambridge university press, 2010.
- [28] C. Liu, C. Zhou, W. Wang, and H. Zhang, "Bimetallic microswimmers speed up in confining channels," *Phys. Rev. Lett.*, vol. 117, no. 19, p. 198001, 2016.
- [29] G. Wei, D. Renfeng, T. Soracha, L. Jinxing, G. Weiwei, Z. Liangfang, and W. Joseph, "Artificial micromotors in the mouse's stomach: A step toward in vivo use of synthetic motors," *ACS Nano*, vol. 9, no. 1, p. 117123, 2015.
- [30] L. Soler, C. Martínez-Cisneros, A. Swiersy, S. Sánchez, and O. G. Schmidt, "Thermal activation of catalytic microjets in blood samples using microfluidic chips," *Lab on a Chip*, vol. 13, no. 22, pp. 4299–4303, 2013.
- [31] X. Ma, A. C. Hortelão, T. Patiño, and S. Sánchez, "Enzyme catalysis to power micro/nanomachines," *ACS nano*, vol. 10, no. 10, pp. 9111–9122, 2016.
- [32] W. Gao, S. Sattayasamitsathit, J. Orozco, and J. Wang, "Highly efficient catalytic microengines: template electrosynthesis of polyaniline/platinum microtubes," *J. Am. Chem. Soc.*, vol. 133, no. 31, pp. 11 862–11 864, 2011.
- [33] J. R. Baylis, J. H. Yeon, M. H. Thomson, A. Kazerooni, X. Wang, A. E. St. John, E. B. Lim, D. Chien, A. Lee, J. Q. Zhang, J. M. Piret, L. S. Machan, T. F. Burke, N. J. White, and C. J. Kastrop, "Self-propelled particles that transport cargo through flowing blood and halt hemorrhage," *Science Advances*, vol. 1, no. 9, pp. 1–8, 2015.
- [34] J. Burdick, R. Laocharoensuk, P. M. Wheat, J. D. Posner, and J. Wang, "Synthetic nanomotors in microchannel networks: Directional microchip

motion and controlled manipulation of cargo," *J. Am. Chem. Soc.*, vol. 130, no. 26, pp. 8164–8165, 2008.